Guided wave dispersion curves for a bar with an arbitrary cross-section, a rod and rail example.

Takahiro Hayashi, Won-Joon Song and Joseph L. Rose

Corresponding author; T. Hayashi

Department of Mechanical Engineering, Nagoya Institute of Technology

Gokiso Showa Nagoya, 466-8555 Japan

+81-52-735-5338(voice), +81-52-735-5342(fax)

a) Electronic-mail: hayashi@megw.mech.nitech.ac.jp

Abstract

Theoretical and experimental issues of acquiring dispersion curves for bars of arbitrary cross-section are discussed. Since a guided wave can propagate over long distances in a structure, guided waves have great potential for being applied to the rapid nondestructive evaluation of large structures such as rails in the railroad industry. Such fundamental data as phase velocity, group velocity, and wave structure for each guided wave mode is presented for structures with complicated cross-sectional geometries as rail. Phase velocity and group velocity dispersion curves are obtained for bars with an arbitrary cross-section using a semi-analytical finite element method (SAFE). Since a large number of propagating modes with close phase velocities exist, dispersion curves consisting of only dominant modes are obtained by calculating the displacement at a received point for each mode. These theoretical dispersion curves agree in characteristic parts with the experimental dispersion curves obtained by a two-dimensional Fourier transform technique.

PACS numbers: 43.20. Jr,, 43.20. Mv.

Keywords; guided wave, dispersion curve, semi-analytical finite element method, two-dimensional Fourier transform, rail inspection

1. Introduction

Guided wave ultrasonic modes propagating over long distances along large bar or plate-like structures are useful in rapid long-range nondestructive evaluation. Guided waves have already been applied to a wide variety of NDE for plate-like structures. Recently, applications to pipe and rail inspection have attracted considerable attention [1-4]. Dispersion curves, representing frequency dependence of guided wave velocities, are indispensable for such guided wave NDE. Dispersion curves present fundamental information on guided waves such as wavelength and dispersivity as well as phase and group velocities at a certain frequency. Such fundamental information plays an important role in determining incident and receiving angles of angle beam transducers and spacing of comb type transducers such as EMATs and PVDF films and to estimate also the traveling time of each mode. Therefore, dispersion curves are theoretically obtained initially followed by actual guided wave measurements [5].

Theoretical studies on dispersion curves for guided waves have been carried out for over one hundred years; Pochhammer [6] and Chree [7] first developed the results for rods and Rayleigh and Lamb presented them for plates. Then, Davis [8] presented many theoretical and experimental investigations. The other early work was carried out by such famous individuals as Mindlin [9], Onoe [10], Gazis [11], Viktorov [12], Graff [13], Auld [14] and Achenbach [15].

As for such simple structures as plates, solid rods and hollow cylinders, detailed investigations have been given on wave structures for each mode and for reflection, transmission and scattering characteristics of guided waves as well [16-19]. Furthermore, complicated guided wave motions have been revealed by computer simulations and

visualization [20]. In these numerical analyses, specialized calculation techniques were developed so that guided wave propagating over long distances could be expressed, such as the hybrid method of the normal expansion theory and the FEM or BEM and the semi-analytical finite element method (SAFE) where wave motions in the propagation direction are theoretically treated and the cross-section is sub-divided.

As for a bar with an arbitrary cross-section, Nigro [21] and Aalami [22] gave approximate solutions using the Rayleigh-Ritz method and showed dispersion curves for such simple geometries as square and rectangular bars. Recently, Taweel *et. al*. [23] presented that these solutions are obtainable by the SAFE. Gavrić [24], Gry [25] and Thompson and Jones[26] studied dispersion curves for a rail for the purpose of noise reduction. However, there is little study on guided waves in bars with a complicated cross-sectional geometry such as a rail for the purpose of ultrasonic non-destructive evaluation. Thus, fundamental information on guided waves is required so as to adapt for ultrasonic guided waves into a complicated cross-sectional bar.

Thus, the purpose of this study is to obtain theoretical phase and group velocity dispersion curves and to verify them experimentally, in order to apply ultrasonic guided waves to NDE for bars with a complex cross-section. First, the approximate solutions of the phase velocity dispersion curves by the SAFE are described, and then the derivations of the group velocity dispersion curves and displacements at any location are presented. Theoretical dispersion curves for a square rod and rail, however, show a large number of propagating modes with close phase velocities, which are generally not useful for practical NDE applications. Therefore, dispersion curves are represented by shading depending on the displacement at a receiver point. Finally, these theoretical dispersion

curves, consisting of only dominant modes, are compared with experimental dispersion curves obtained by the two-dimensional Fourier transform technique.

2. Semi-analytical FEM

A. Governing equations

In Lamb wave calculations by the SAFE method, assuming plain strain, a cross-section of a plate is divided in the thickness direction into layered elements, and waves in the propagating direction *z* are described by the orthogonal function $\exp(i\xi z)$ where ξ is the wavenumber of the Lamb wave. The *m*th eigenvalue ξ_m of the eigensystem derived here denotes the wavenumber of the *m*th resonance mode. In the case of a bar with an arbitrary cross-section, the two dimensional cross-section is sub-discritized and waves in the longitudinal direction *z* are described by the orthogonal function $\exp(i\xi z)$. Similarly, wavenumbers are obtained as the eigenvalues ξ_m of the eigensystem, and then dispersion curves can be depicted.

First, consider a quadratic prism element that consists of a small quadrilateral on a cross-sectional *x*-*y* plane and straight edges in the *z* direction. When the displacement, strain, stress and external traction vectors at any point (*x*, *y*, *z*) in this element are written as

$$\mathbf{u} = \begin{bmatrix} u_x & u_y & u_z \end{bmatrix}^T \tag{1}$$

$$\boldsymbol{\varepsilon} = \begin{bmatrix} \varepsilon_{xx} & \varepsilon_{yy} & \varepsilon_{zz} & \gamma_{yz} & \gamma_{zx} & \gamma_{xy} \end{bmatrix}^T \tag{2}$$

$$\boldsymbol{\sigma} = \begin{bmatrix} \sigma_{xx} & \sigma_{yy} & \sigma_{zz} & \sigma_{yz} & \sigma_{zx} & \sigma_{xy} \end{bmatrix}^T \tag{3}$$

$$\mathbf{t} = \begin{bmatrix} t_x & t_y & t_z \end{bmatrix}^T, \tag{4}$$

the virtual work principle gives the following governing equations,

$$\int_{\Gamma} \delta\mathbf{u}^T \mathbf{t}\ d\Gamma = \int_{V} \delta\mathbf{u}^T \left(\rho\ddot{\mathbf{u}}\right)\ dV + \int_{V} \delta\boldsymbol{\varepsilon}^T \boldsymbol{\sigma}\ dV \tag{5}$$

where T denotes transposed or Hermitian matrices, ρ is density and $\ddot{\bullet}$ is a second differentiation with respect to time *t*. $\int_{\Gamma} \bullet\, d\Gamma$ and $\int_{V} \bullet\, dV$ are the surface integration on the outer surface of the prismatic element and the volume integration of the element, respectively. The left hand side denotes the work done by the external traction **t**, and the first and second term of the right hand side are the increment of kinetic energy and potential energy, respectively.

Now, considering the harmonic wave $\exp(-i\omega t)$, the displacement vector at an arbitrary point Eq.(1) can be written as,

$$\mathbf{u} = \mathbf{N}(x, y)\mathbf{U}^j(z)\exp(-i\omega t) \tag{6}$$

where $\mathbf{N}(x, y)$ is the interpolation function, and $\mathbf{U}^j(z)$ is the nodal displacement vector of the *j*th element. For four node elements, $\mathbf{N}(x, y)$ is a 3x12 matrix and $\mathbf{U}^j(z)$ is a 12 element vector. Since $\mathbf{U}^j(z)$ is a function of *z*, this can be rewritten by the Fourier transform as,

$$\mathbf{U}^j(z) = \int_{-\infty}^{+\infty} \overline{\mathbf{U}}^j \exp(i\xi z)\ d\xi\ . \tag{7}$$

Now considering a certain wavenumber ξ, the displacement vector at an arbitrary point in the *j*th element is

$$\mathbf{u} = \mathbf{N}(x, y)\overline{\mathbf{U}}^j \exp(i\xi z - i\omega t)\,. \tag{8}$$

The strain vector is written by the strain-displacement relation as,

$$\boldsymbol{\varepsilon} = \left[\mathbf{L}_x \frac{\partial}{\partial x} + \mathbf{L}_y \frac{\partial}{\partial y} + \mathbf{L}_z \frac{\partial}{\partial z} \right] \mathbf{u} \tag{9}$$

$$\mathbf{L}_x = \begin{bmatrix} 1 & 0 & 0 \\ 0 & 0 & 0 \\ 0 & 0 & 0 \\ 0 & 0 & 0 \\ 0 & 0 & 1 \\ 0 & 1 & 0 \end{bmatrix}, \ \mathbf{L}_y = \begin{bmatrix} 0 & 0 & 0 \\ 0 & 1 & 0 \\ 0 & 0 & 0 \\ 0 & 0 & 1 \\ 0 & 0 & 0 \\ 1 & 0 & 0 \end{bmatrix}, \ \mathbf{L}_z = \begin{bmatrix} 0 & 0 & 0 \\ 0 & 0 & 0 \\ 0 & 0 & 1 \\ 0 & 1 & 0 \\ 1 & 0 & 0 \\ 0 & 0 & 0 \end{bmatrix}. \tag{10}$$

Substituting Eq.(8) into Eq.(9) gives

$$\boldsymbol{\varepsilon} = \left(\mathbf{B}_1 + i\xi \mathbf{B}_2 \right) \overline{\mathbf{U}}^j \exp\left(i\xi z - i\omega t \right) \tag{11}$$

$$\mathbf{B}_1 = \mathbf{L}_x \mathbf{N}_{,x} + \mathbf{L}_y \mathbf{N}_{,y}, \quad \mathbf{B}_2 = \mathbf{L}_z \mathbf{N} \tag{12}$$

, where $\mathbf{N}_{,x}$ and $\mathbf{N}_{,y}$ are the differentiation of the interpolation function **N** with respect to *x* and *y*, respectively. The stress vector $\boldsymbol{\sigma}$ is written by the stress-strain relation as

$$\boldsymbol{\sigma} = \mathbf{c}\boldsymbol{\varepsilon} \tag{13}$$

, where **c** is an elastic coefficient matrix. Similarly to the displacement vector **u** in Eq.(8), the external traction vector **t** is described using the nodal external traction vector $\overline{\mathbf{T}}^j$ as,

$$\mathbf{t} = \mathbf{N}\overline{\mathbf{T}}^j \exp\left(i\xi z - i\omega t \right). \tag{14}$$

Substituting Eqs.(8), (11), (13) and (14) in Eq.(5) and rearranging this gives

$$\mathbf{f}^j = \left(\mathbf{K}_1{}^j + i\xi \mathbf{K}_2{}^j + \xi^2 \mathbf{K}_3{}^j \right) \overline{\mathbf{U}}^j - \omega^2 \mathbf{M}^j \overline{\mathbf{U}}^j \tag{15}$$

$$\left.\begin{aligned} \mathbf{f}^j &= \int_{\Gamma'} \mathbf{N}^T \mathbf{N} \overline{\mathbf{T}}^j d\Gamma' \\ \mathbf{K}_1{}^j &= \int_y \int_x \mathbf{B}_1{}^T \mathbf{c} \mathbf{B}_1 dxdy \\ \mathbf{K}_2{}^j &= \int_y \int_x \left(\mathbf{B}_1{}^T \mathbf{c} \mathbf{B}_2 - \mathbf{B}_2{}^T \mathbf{c} \mathbf{B}_1 \right) dxdy \\ \mathbf{K}_3{}^j &= \int_y \int_x \mathbf{B}_2{}^T \mathbf{c} \mathbf{B}_2 dxdy \end{aligned}\right\} \tag{16}$$

$$\mathbf{M}^j = \int_y \int_x \rho \mathbf{N}^T \mathbf{N} dx dy$$

, where Γ' stands for the boundary of the cross-section. Numerical integration gives the values in Eq.(16). Calculating Eq.(16) for all elements and overlapping the values with respect to the common nodes results in the following governing equations for the total system.

$$\mathbf{f} = \left(\mathbf{K}_1 + i\xi\mathbf{K}_2 + \xi^2\mathbf{K}_3\right)\overline{\mathbf{U}} - \omega^2\mathbf{M}\overline{\mathbf{U}} \tag{17}$$

, where $\mathbf{K}_1$, $\mathbf{K}_2$, $\mathbf{K}_3$ and $\mathbf{M}$ are the MxM matrices determined by the geometry and **f** is the nodal force vector given by the boundary conditions (Mx1; M is three times the number of nodes). $\overline{\mathbf{U}}$ is the unknown nodal displacement vector. Eq.(17) can be rewritten as the following eigensystem with a first-order wavenumber ξ.

$$\left(\mathbf{A} - \xi\mathbf{B}\right)\mathbf{Q} = \mathbf{p} \tag{18}$$

$$\left.\begin{aligned} \mathbf{A} &= \begin{bmatrix} 0 & \mathbf{K}_1 - \omega^2\mathbf{M} \\ \mathbf{K}_1 - \omega^2\mathbf{M} & i\mathbf{K}_2 \end{bmatrix} \\ \mathbf{B} &= \begin{bmatrix} \mathbf{K}_1 - \omega^2\mathbf{M} & 0 \\ 0 & -\mathbf{K}_3 \end{bmatrix} \\ \mathbf{Q} &= \begin{bmatrix} \overline{\mathbf{U}} \\ \xi\overline{\mathbf{U}} \end{bmatrix}, \qquad \mathbf{p} = \begin{bmatrix} 0 \\ \mathbf{f} \end{bmatrix} \end{aligned}\right\} \tag{19}$$

Assuming **p**=0, the eigenvalue ξ_m (m=1,2…2M) of the eigensystem Eq.(18) corresponds to the mth wavenumber of the guided wave modes satisfying the resonant condition of this bar. Phase velocity of the mth mode at frequency ω is given by $c_m = \omega/\xi_m$. These eigenvalues consist of wavenumbers for both M forward waves and M backward waves. When ξ_m is a complex number, the mth mode is an evanescent mode, and for real ξ_m, the

*m*th mode is a propagating mode. For the propagating modes, the sign of group velocity determines whether it is a forward wave or a backward wave. Since the sign of phase velocity and group velocity can be opposite in certain frequency range values, the propagating direction cannot be decided by the sign of the phase velocity. From Eq.(18), moreover, 2M left eigenvectors $\mathbf{\Phi}^L{}_m$ (1x2M vector) and 2M right eigenvectors $\mathbf{\Phi}^R{}_m$ (2Mx1) are obtained.

B. Group velocity

The group velocity of the *m*th mode is written as $c_{g_m} = d\omega/d\xi_m$. Therefore, in order to calculate the group velocity at a frequency ω, the wavenumber $\xi_m + \Delta\xi_m$ at the frequency $\omega + \Delta\omega$ must be obtained, as well as the wavenumber ξ_m at the frequency ω. The wavenumber $\xi_m + \Delta\xi_m$ can be calculated at the frequency $\omega + \Delta\omega$ by the technique described above. Since the differentiation is executed by the two wavenumbers $\xi_m + \Delta\xi_m$ and ξ_m corresponding to the same mode, the vibration mode must be identified correctly. This is very difficult in this case where many modes with close wavenumbers are possible. Moreover, a small error in the wavenumbers causes large errors in the differentiation of group velocity. Therefore, group velocity should be obtained theoretically.

Suppose that matrices $\mathbf{A}$ and $\mathbf{B}$ become $\mathbf{A} + \Delta\mathbf{A}$ and $\mathbf{B} + \Delta\mathbf{B}$ at the frequency $\omega + \Delta\omega$, and that eigenvalue and left and right eigenvectors are obtained as $\xi_m + \Delta\xi_m$, $\mathbf{\Phi}^L{}_m + \Delta\mathbf{\Phi}^L{}_m$ and $\mathbf{\Phi}^R{}_m + \Delta\mathbf{\Phi}^R{}_m$, respectively. Then, the following eigensystem is satisfied.

$$\{(\mathbf{A}+\Delta\mathbf{A})-(\xi_m+\Delta\xi_m)(\mathbf{B}+\Delta\mathbf{B})\}(\mathbf{\Phi}^R{}_m+\Delta\mathbf{\Phi}^R{}_m)=0 \tag{20}$$

Removing the second-order differential term and rearranging Eq.(20) give

$$(\mathbf{A}-\xi_m\mathbf{B})\Delta\mathbf{\Phi}^R{}_m=(-\Delta\mathbf{A}+\xi_m\Delta\mathbf{B}+\Delta\xi_m\mathbf{B})\mathbf{\Phi}^R{}_m \tag{21}$$

Now, since $\mathbf{\Phi}^R{}_m$ is an orthogonal vector, $\Delta\mathbf{\Phi}^R{}_m$ can be written as the superposition of $\mathbf{\Phi}^R{}_l$ (l=1,2… 2M) as,

$$\Delta\mathbf{\Phi}^R{}_m=\sum_{l=1}^{2M}\mathbf{\Phi}^R{}_l C_{lm}\,. \tag{22}$$

where C_{lm} is an arbitrary constant. Substituting Eq.(22) in Eq.(21) gives

$$(\mathbf{A}-\xi_m\mathbf{B})\sum_{l=1}^{2M}\mathbf{\Phi}^R{}_l C_{lm}=(-\Delta\mathbf{A}+\xi_m\Delta\mathbf{B}+\Delta\xi_m\mathbf{B})\mathbf{\Phi}^R{}_m \tag{23}$$

Multiplying $\mathbf{\Phi}^L{}_m$ from the left of Eq.(23), Eq.(23) can be rewritten as

$$\begin{aligned}&\sum_{l=1}^{2M}\mathbf{\Phi}^L{}_m(\mathbf{A}-\xi_m\mathbf{B})\mathbf{\Phi}^R{}_l C_{lm}\\&=\mathbf{\Phi}^L{}_m(-\Delta\mathbf{A}+\xi_m\Delta\mathbf{B}+\Delta\xi_m\mathbf{B})\mathbf{\Phi}^R{}_m\end{aligned} \tag{24}$$

Considering the following orthogonal condition

$$\mathbf{\Phi}^L{}_m\mathbf{A}\mathbf{\Phi}^R{}_l=\begin{cases}0 & l\neq m\\ \mathbf{\Phi}^L{}_m\mathbf{A}\mathbf{\Phi}^R{}_m & l=m\end{cases} \tag{25}$$

$$\mathbf{\Phi}^L{}_m\mathbf{B}\mathbf{\Phi}^R{}_l=\begin{cases}0 & l\neq m\\ \mathbf{\Phi}^L{}_m\mathbf{B}\mathbf{\Phi}^R{}_m & l=m\end{cases} \tag{26}$$

$$\mathbf{\Phi}^L{}_m\mathbf{A}\mathbf{\Phi}^R{}_m=\xi_m\mathbf{\Phi}^L{}_m\mathbf{B}\mathbf{\Phi}^R{}_m \tag{27}$$

, the left hand side of Eq.(24) becomes zero. Eq.(24) results in

$$\Delta\xi_m=\frac{\mathbf{\Phi}^L{}_m(\Delta\mathbf{A}-\xi_m\Delta\mathbf{B})\mathbf{\Phi}^R{}_m}{\mathbf{\Phi}^L{}_m\mathbf{B}\mathbf{\Phi}^R{}_m}\,. \tag{28}$$

This equation indicates that we can estimate the wavenumber of the *m*th mode $\xi_m + \Delta\xi_m$ at the frequency $\omega + \Delta\omega$ by the use of the wavenumber of the *m*th mode ξ_m and the left and right eigenvector $\mathbf{\Phi}^L{}_m$, $\mathbf{\Phi}^R{}_m$ at the frequency ω. This leads to group velocity c_{g_m} at the frequency ω for the *m*th mode.

C. Displacement field

The solution of Eq.(18) is obtained as

$$\mathbf{Q} = \sum_{m=1}^{2M} Q_m \mathbf{\Phi}^R{}_m \ . \tag{29}$$

$$Q_m = -\frac{\mathbf{\Phi}^L{}_m \mathbf{p}}{(\xi - \xi_m) B_m}, \quad B_m = \mathbf{\Phi}^L{}_m \mathbf{B} \mathbf{\Phi}^R{}_m \tag{30}$$

Since the nodal displacement vector $\overline{\mathbf{U}}$ (Mx1 vector) is the upper part of $\mathbf{Q}$ (2Mx1 vector),

$$\overline{\mathbf{U}} = \sum_{m=1}^{2M} Q_m \mathbf{\Phi}^{Rup}{}_m \tag{31}$$

where $\mathbf{\Phi}^{Rup}{}_m$ is the upper part of $\mathbf{\Phi}^R{}_m$.

Here we consider point loading on the outer surface at $z=z_S$. Eq.(30) can be written as

$$Q_m = -\frac{\mathbf{\Phi}^L{}_m \mathbf{p}}{(\xi - \xi_m) B_m} \delta(z - z_S) \tag{32}$$

, where **p** is the vector given by Eq.(19), having nodal force values only in the components corresponding to the loaded nodes. Since the displacement vector $\mathbf{U}$ is the Fourier transform with respect to the wavenumber ξ as given in Eq.(7), substituting Eq.(31) in Eq.(7) and applying the residual theorem gives

$$\mathbf{U} = \sum_{m=1}^{M} \alpha_m \mathbf{\Phi}^{Rup}{}_m \exp\{i\xi_m (z - z_S)\} \tag{33}$$

$$\alpha_m = -\frac{\mathbf{\Phi}^{L}{}_m \mathbf{p}}{B_m}, \tag{34}$$

where, for $z > z_S$, Eq.(33) is expressed as the superposition of M forward waves, while for $z < z_S$, Eq.(33) becomes the superposition of M backward waves. The nodal displacement is obtained by Eq.(33), and then the displacement at an arbitrary point is calculated by the use of interpolation function **N**.

3. Dispersion curves for a square rod

Iterating the calculation of eigenvalues ξ_m at every frequency leads to the phase velocity dispersion curves. Calculating the increment of the wavenumber $\Delta\xi_m$ written by Eq.(28) at every frequency step provides us with the group velocity dispersion curves. Here we investigate the accuracy of this calculation technique by examining dispersion curves with various numbers of elements for a square rod. Figure 1 shows the phase velocity (a) and group velocity (b) dispersion curves calculated with various numbers of elements for a material with Poisson's ratio ν=0.30, where *f* is frequency, *h* is the length of the side of a square cross-section and *c*, c_g, c_T denote phase velocity, group velocity and transverse wave velocity, respectively. As the number of elements increases, dispersion curves for all modes shift to lower frequency and lower phase velocity values, and then converge. In the *fh* region below 2.5MHzmm, curves converge with 12x12 elements, which means that the SAFE calculation is carried out with sufficient accuracy. In the higher frequency range and for higher order modes, however, the curves do not

converge even with 12x12 elements. However, we notice the tendency that these curves shifts toward the low frequency and low phase velocity region (low wavenumber direction) and then converges when the elements increase. Thus, satisfactory dispersion curves can be obtained even with reduced number of elements.

In the low frequency range below 2MHz mm shown in Fig.1, three propagating modes exist; the fundamental symmetric (S0), fundamental anti-symmetric (A0) and shear horizontal mode (SH). These were described in detail in previous papers as the longitudinal, flexural and torsional mode[19,20]. The torsional mode is almost a straight line as seen in the dispersion curves of guided waves in plates or hollow cylinders, but it should be noted that its velocity c is slightly smaller than the transverse velocity c_T ($c/c_T \cong 0.92$). These lower order modes given by the SAFE calculation agree well with values in the previous papers [19,20].

Next, experimental dispersion curves are obtained for the steel rod (c_L=5.85mm/μs, c_T=3.23mm/μs). The contact transducer (center frequency 50kHz) mounted on the upper surface of the square bar (h=5.08mm, about 2.5m length) excited tone burst signals from the edge of the bar. A non-contact air-coupled transducer (Ultran, 60kHz) enables us to measure waveforms with rapid scanning over the bar. This sensor was set at the vibrating surface of the air-coupled transducer, parallel to the upper surface of the square bar with about a 30mm spacing. Waveforms were recorded at 200 locations from L=0.3m to L=2.3m in 10mm increment, where L denotes the distance between the contact transmitter and the air-coupled receiver. Since waveforms were stored from t=0 to 12.8ms, highly dispersive modes with very low group velocity values were detected as well as fast modes reflecting iteratively between two edge of the bar. In the two

dimensional FFT, two dimensional discrete data in the time direction and in the spatial direction are converted into those in the frequency domain and in the wavenumber domain, respectively. Figure 2 shows the experimental dispersion curves (a)(c) and the theoretical dispersion curves by the SAFE with 12x12 elements (b)(d)(e); (a) and (b) are wavenumber ξ x frequency f representations and (c),(d) and (e) are frequency f x phase velocity c representations. In fig. 2 (c), phase velocity c is obtained by the relation $c=\omega/\xi$ using wavenumber ξ given in fig.2 (a). Therefore, phase velocity below $c_{\min} = \omega/\xi_{\max}$ cannot be obtained, where $\xi_{\max}$ is the maximum value of the wavenumber which is given by the increment of the measurement points dz (=10mm) as $\xi_{\max}=1/2dz$. Since the mode with the lowest phase velocity can be seen in the frequency range considered here, the spatial increment of 10mm was sufficiently small. In the experimental dispersion curves (a)(c), darker dots denote larger amplitude where the amplitude data are normalized by the maximum amplitude at each frequency. Therefore, the results around the center frequency of 50kHz are less influenced by noise and more reliable than those as we move further away from 50kHz. However, the flexural mode from c=0-3.0mm/μs and f=0-20kHz and the higher modes around 100kHz can be clearly seen in Fig.2(c). The darker regions in the experimental results agree well with the theoretical solutions (b)(d) in the SAFE calculations, which verifies the SAFE calculations.

However, all curves obtained in the SAFE calculation do not appear in the experimental dispersion curves. For instance, the shear horizontal mode and the longitudinal mode in a low frequency region cannot be seen because the air-coupled transducer does not detect such in-plain modes. Especially in the higher frequency range,

many higher order modes exist in the SAFE calculation results (b)(d). Thus, it is not easy to verify the dispersion curves given by the SAFE calculation from the experimental results. Therefore, to remove modes that cannot be measured and to highlight largely influential modes, dispersion curves are plotted by amplitudes at a measured point for each mode when point load is applied at the upper surface of the rod (Fig.2 (e)). The shading in Fig.2 (e) is similar to the experimental results; e.g., highly dispersive modes around 55, 65 and 85kHz agree well with Fig.2(c).

4. Dispersion curves for a rail

Next, dispersion curves are plotted by the SAFE calculation for a practical rail structure. A cross-section and sub-divisions of a rail are shown in Fig.3. The number of elements is 68, which may be insufficient to obtain the exact solutions, but we can roughly estimate the dispersion curves as shown in the previous section. Phase velocity and group velocity dispersion curves for the rail given are given by the SAFE calculation as Fig.4. Since many modes exist in this frequency range, these dispersion curves are not useful for guided wave analyses. Similarly to the square rod, however, many modes should be removed by considering the measurement conditions.

In order to obtain experimental dispersion curves, waveforms were collected at many regularly spaced locations as in the square rod tests. The length of the rail was about 2.4m and the cross-section is shown as Fig.3. The contact transmitter was located on the upper surface of the head part and the non-contact air-coupled receiver was set about 30mm away from the upper and lateral surface of the head to detect the out-of-plain displacement on each surface. Waveforms were collected at 200 points in 10mm

increments in the longitudinal direction. Fig.5 shows the waveforms captured at L=0.5m and L=1.5m; L is the intertransducer distance. Phase velocity dispersion curves are shown in Fig.6 by dark dots. Fig.6(a) and (b) are the experimental results from the upper surface and the lateral surface measurements, respectively. In Fig.6 (a), three characteristic modes can be seen; one is a less dispersive mode from c=2.2 mm/μs to 3.0 mm/μs over the frequency range of 5kHz and the other two are highly dispersive modes over 35kHz. In Fig.6 (b), two characteristic modes are shown; one is a less dispersive mode over the frequency range of 5kHz as in Fig.6 (a) and the other one is a highly dispersive mode appearing over the frequency range of 25kHz.

In the dispersion curves by the SAFE calculation (Fig.4), many modes are shown in addition to these characteristic modes. In order to compare the SAFE solutions with the experimental results, dispersion curves are plotted by changing the shading depending on the displacement at the measured point (Fig.6 (c), (d)). These calculation results (c) and (d) agree well with the experimental results Fig.6 (a) and (b), respectively.

Next, Fig.7 (a) and (b) show group velocity dispersion curves plotted depending on the displacement. Both figures indicate that all measured modes are below about 3.2mm/μs and fast modes cannot be seen. Fig.5 shows the waveforms measured at L=0.5m and L=1.5m; L is the intertransducer distance. Since these waveforms appear at 410μs and 720μs, respectively, group velocity is derived to be about 3.2mm/μs from the time difference. This result agrees well with the field tests using a long rail[4]. After the first wave appears, many dispersive modes are mixed. Thus, the waveforms do not give useful information about the propagating path. Therefore, when raw waveforms without

any treatments as 2DFFT are used in NDE of a bar with complicated cross-section, the fastest modes with the group velocity around the transverse velocity are useful.

5. Conclusions

The approximate solutions for phase velocity, group velocity and displacement of guided waves by a semi-analytical finite element method (SAFE) were described in this paper. It was found in convergence tests on the dispersion curves, that the rough approximate curves could be obtained even with a reduced number of elements. Dispersion curves for a square bar and rail were shown. A large number of propagating modes with close phase velocities occur in the dispersion curves especially for a bar with such a complex cross-section as rail. A practical issue of dispersion curve modification was made. Dominant modes were obtained by calculating displacements under the boundary condition that meets the actual measurement set-up, and then dispersion curves were drawn with the dominant modes highlighted. These theoretical dispersion curves agree well with the experimental dispersion curves given by the two-dimensional Fourier transform technique. In the rail structure, three dominant modes were seen in the dispersion curves obtained by measurements on the upper surface of the rail head, while two dominant modes were obtained for measurements on the lateral surface of the rail head. In the SAFE calculations, the group velocities of these dominant modes were predicted to be below about 3.2mm/μs, which was verified by experimental measurements.

Figure Captions

FIG. 1. Dispersion curves for ν=0.30 by the SAFE calculation

(a) phase velocity (b) group velocity

FIG. 2. Comparison between experimental and theoretical dispersion curves for the steel rod

(a) Experimental, wavenumber (ξ) x frequency(f) representation

(b) Theoretical, ξ x f representation

(c) Experimental, frequency (f) x phase velocity (c) representation

(d) Theoretical, f x c representation

(e) Theoretical, f x c representation, dominant modes are highlighted

FIG. 3. Rail geometry and sub-divisions

FIG. 4. Dispersion curves for rail (a) phase velocity, (b) group velocity

FIG. 5. Typical waveforms at L=0.5 and L=1.5 on an upper surface of a rail head

FIG. 6. Experimental and theoretical dispersion curves for a rail

(a) Experimental, upper surface of a rail head

(b) Experimental, lateral surface of a rail head

(c) Theoretical, upper surface of a rail head, dominant modes are highlighted.

(d) Theoretical, lateral surface of a rail head, dominant modes are highlighted.

FIG. 7. Theoretical group velocity dispersion curves

Dominant modes are highlighted.

(a) Upper surface of a rail head

(b) Lateral surface of a rail head

FIG.1

Takahiro HAYASHI

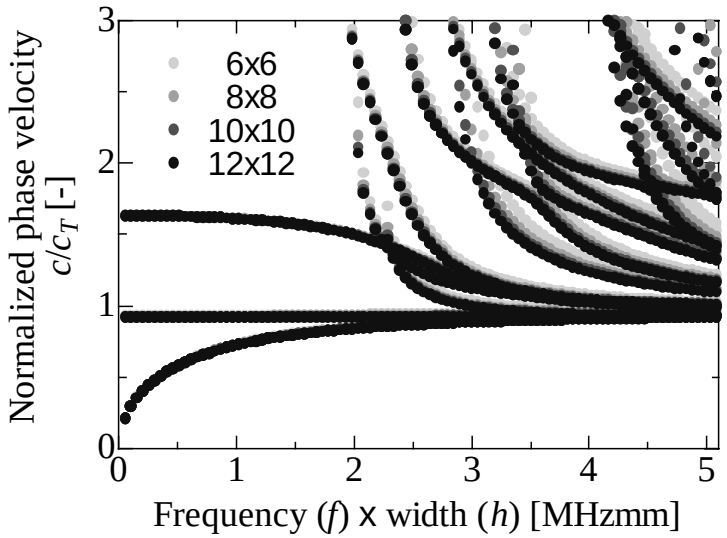

(a) phase velocity

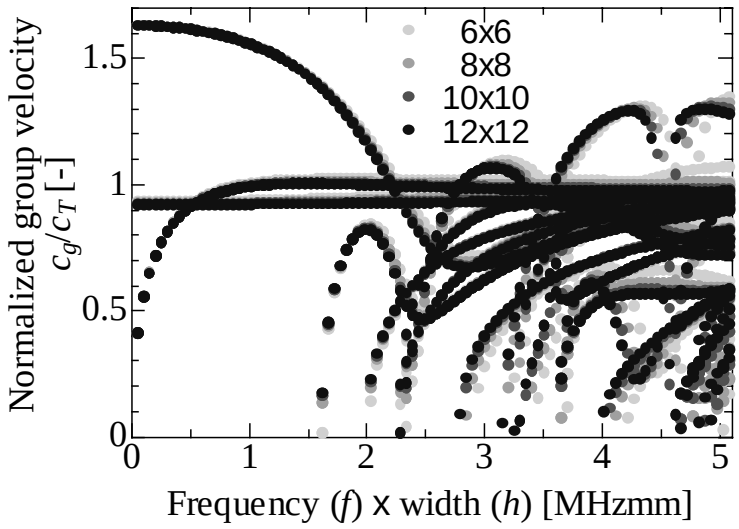

(b) group velocity

FIG.2

Takahiro HAYASHI

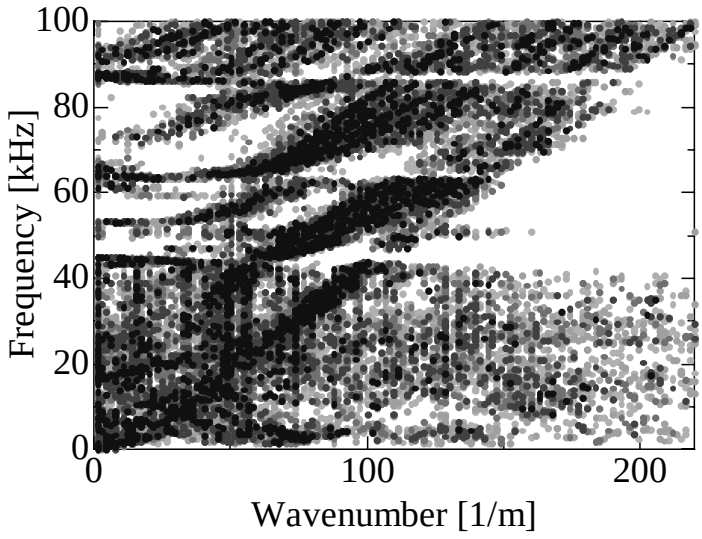

(a) Experimental, wavenumber (ξ) x frequency(f) representation

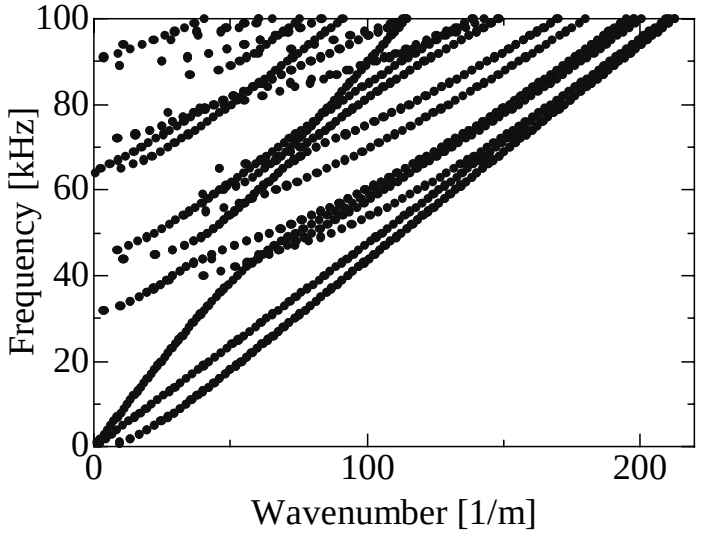

(b) Theoretical, ξ x f representation

FIG.2

Takahiro HAYASHI

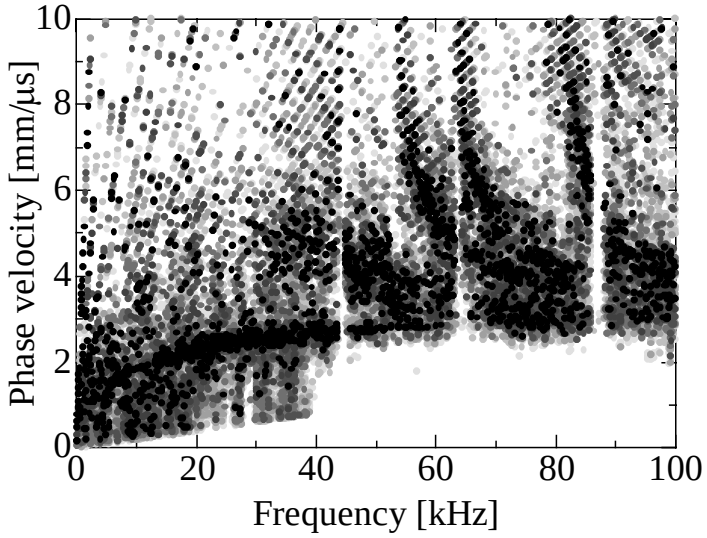

(c) Experimental, frequency (*f*) x phase velocity (*c*) representation

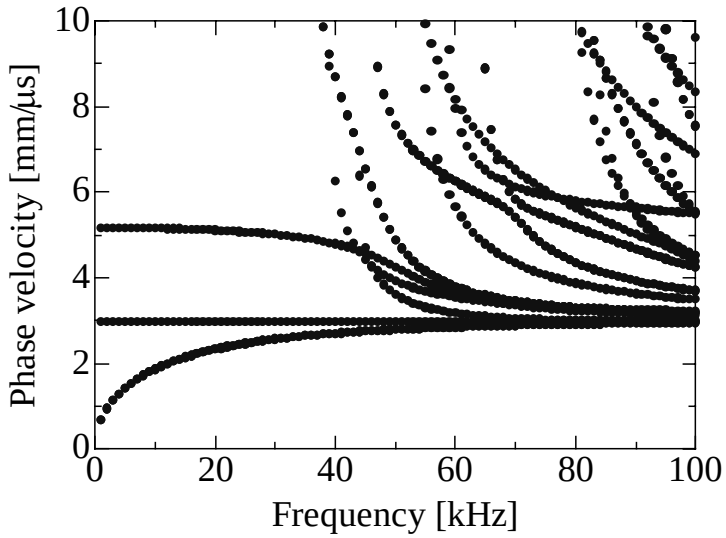

(d) Theoretical, *f* x *c* representation

FIG.2

Takahiro HAYASHI

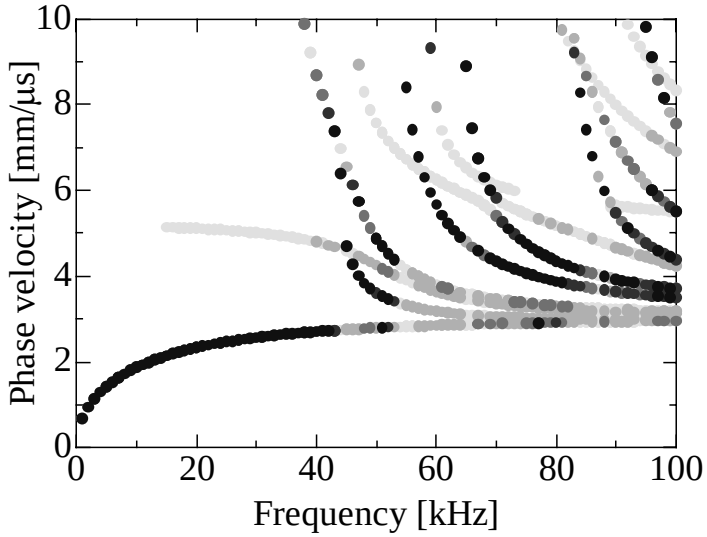

(e) Theoretical, *f* x *c* representation, dominant modes are highlighted

FIG.3

Takahiro HAYASHI

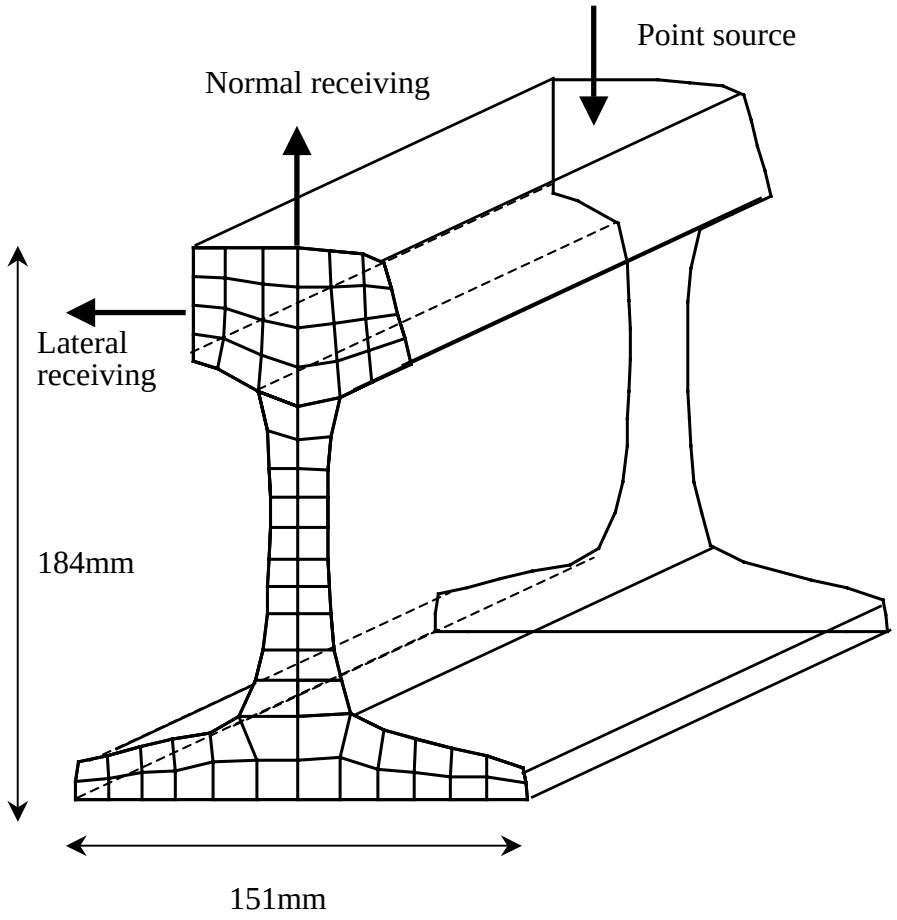

FIG.4

Takahiro HAYASHI

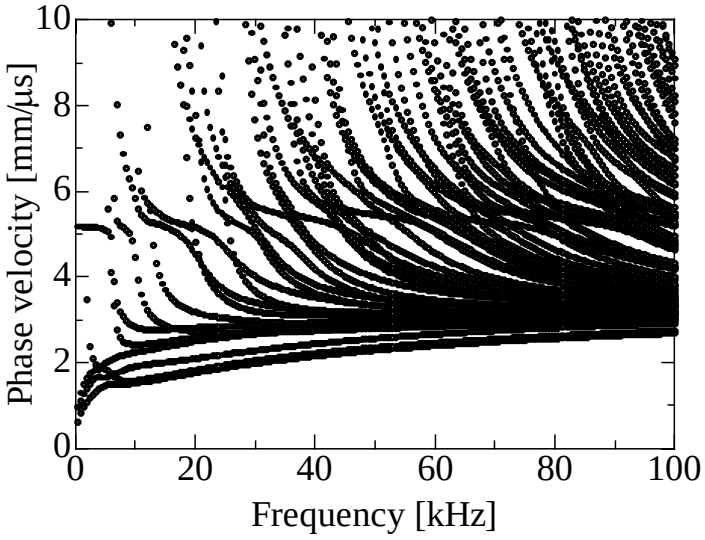

(a) phase velocity

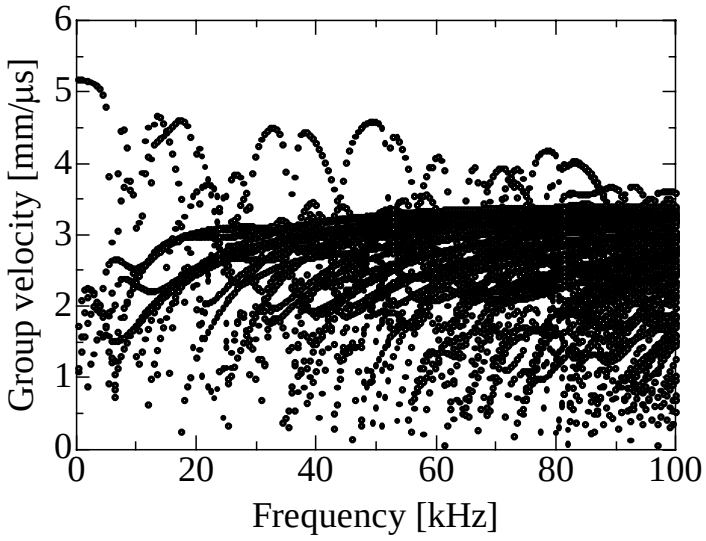

(b) group velocity

FIG.5

Takahiro HAYASHI

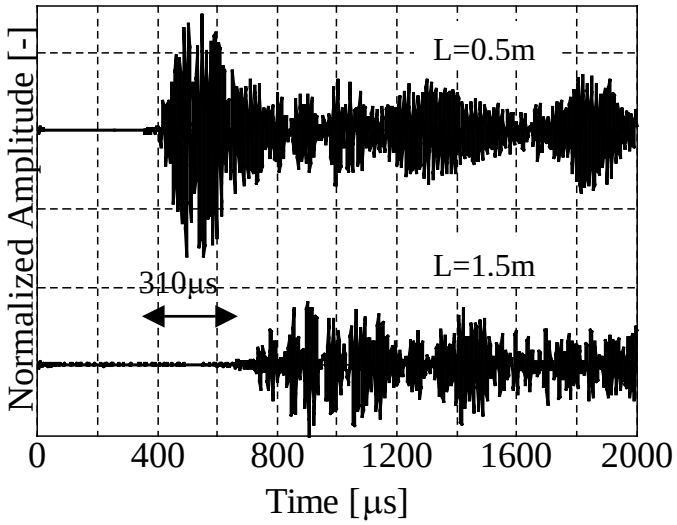

FIG.6

Takahiro HAYASHI

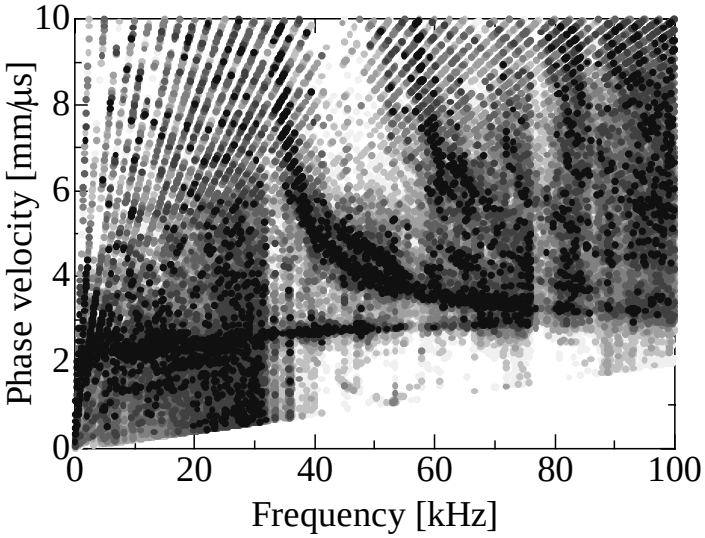

(a) Experimental, upper surface of a rail head

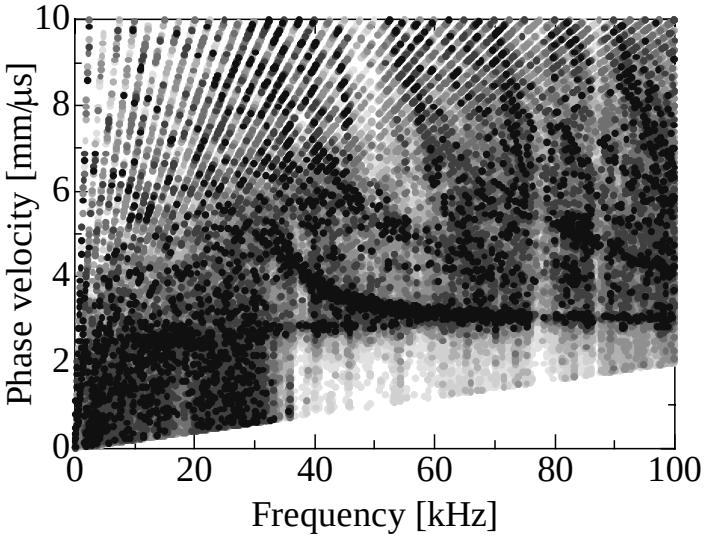

(b) Experimental, lateral surface of a rail head

FIG.6

Takahiro HAYASHI

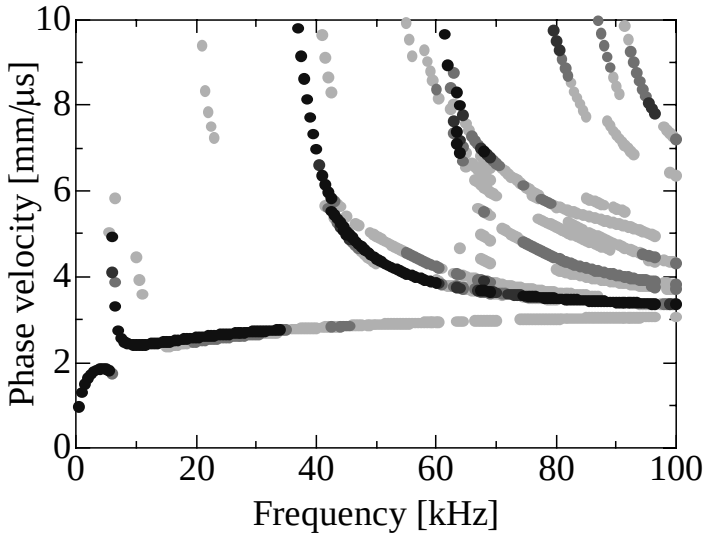

(c) Theoretical, upper surface of a rail head, dominant modes are highlighted

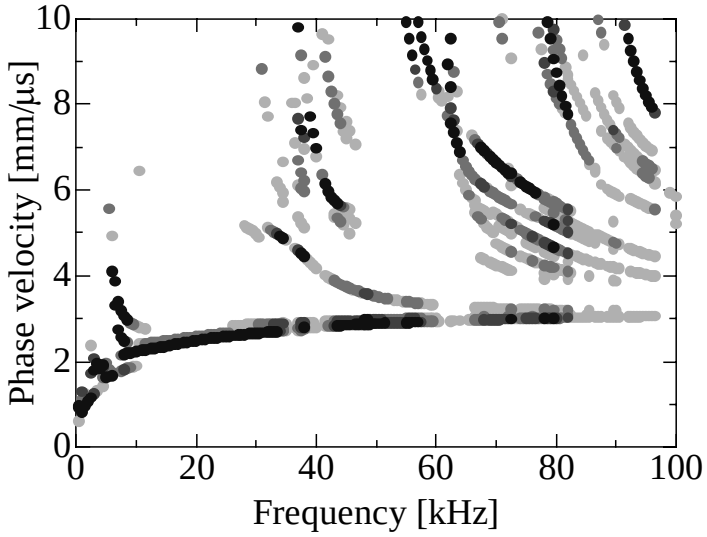

(c) Theoretical, lateral surface of a rail head, dominant modes are highlighted

FIG.7

Takahiro HAYASHI

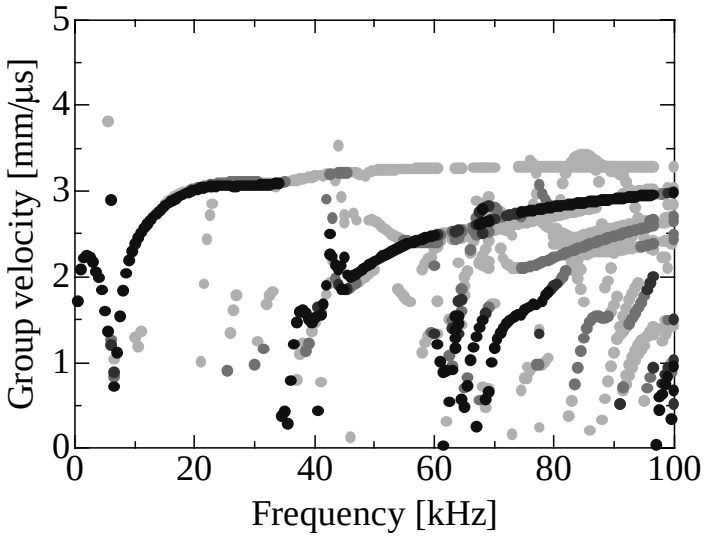

(a) Upper surface of a rail head

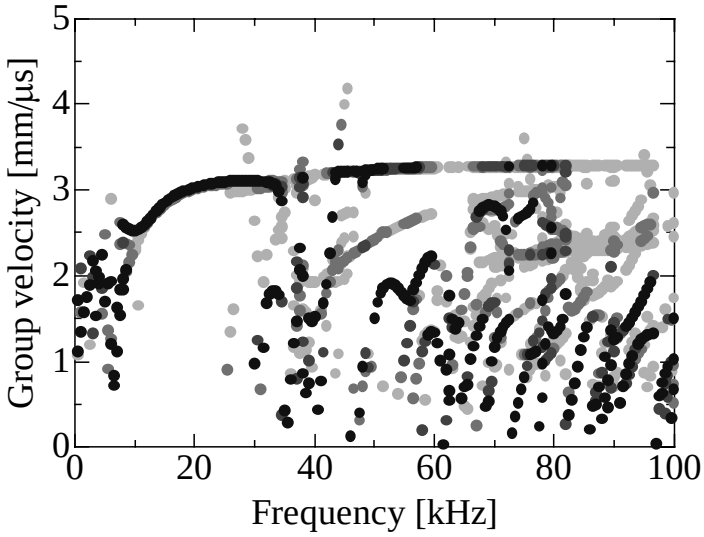

(b) Lateral surface of a rail head

References

[1] D. N. Alleyne, M. J. S. Lowe and P. Cawley, The Reflection of Guided Waves From Circumferential Notches in Pipes, J. Appl. Mech., **65**, 635-641 (1998)

[2] H. J. Shin and J. L. Rose, Guided waves by axisymmetric and non-axisymmetric surface loading on hollow cylinders, Ultrasonics, **37**, 355-363 (1999)

[3] T. Hayashi, K. Kawashima, Z. Sun and J. L. Rose, Analysis of flexural mode focusing by a semi-analytical finite element method, J. Acoust. Soc. Am., Submitted.

[4] J. L. Rose, M. J. Avioli and W.-J. Song, Application and potential of guided wave rail inspection, Insight, 44, 6 353-358 (2002)

[5] J. L. Rose, *Ultrasonic Waves in Solid Media* (Cambridge University Press, 1999)

[6] L. Pochhammer, Über die Fortpflanzungsgeschwindigkeiten kleiner Schwingenungen in einem unbegrenzten isotropen Kreiszylinder, Zeitschrift für reine und angewandte Matematik, **81**, 325-336 (1876)

[7] C. Chree, The equations of an isotropic elastic solid in polar and cylindrical coordinates their solutions and applications, Trans. Cambridge Phil. Soc., **14**, 250-369 (1889)

[8] R. M. Davis, A critical study of the Hopkinson pressure bar, Phil. Trans. R. Soc., **A240**, 375-457 (1948)

[9] R. D. Mindlin, Waves and vibrations in isotropic, elastic plates, Structural Mechanics, edited by J. N. Goodir and N. Hoff (Pergamon Press, Oxford 1959), 199-232

[10] M. Onoe, Contour vibrations of thin rectangular plates, J. Acoust. Soc. Am., **30**, 12, 1159 (1962)

[11] D. C. Gazis, Three-Dimensional Investigation of the Propagation of Waves in Hollow Circular Cylinders. I. Analytical Foundation and II Numerical Results, J. Acoust. Soc. Am., **31** (5), 568-578 (1959)

[12] I. A. Victorov, *Rayleigh and Lamb waves* (Plenum Press, New York, 1967)

[13] K. F. Graff, *Wave motion in elastic solids* (Dover, New York, 1991)

[14] B. A. Auld, *Acoustic fields and waves in solids, 2nd ed. Vols. 1 and 2*, (Kreiger, Malabar, Fl. 1990)

[15] J. D. Achenbach, *Wave propagation in elastic solids* (North-Holland, New York,1984)

[16] N. Guo, P. Cawley, The interaction of Lamb waves with delaminations in composite laminates, J. Acoust. Soc. Am., **94**, 4, 2240- 2246 (1993)

[17] Y. Cho, J. L. Rose, A boundary element solution for a mode conversion study on the edge reflection of Lamb waves, J. Acoust. Soc. Am., **99**, 4 2097-2109 (1996)

[18] G. R. Liu, J. D. Achenbach, Strip element method for stress analysis of anisotropic linearly elestic solids, J. Appl. Mech. **62** (1995) 607

[19] J. M. Galán, R. Abascal, Numerical simulation of Lamb wave scattering in semi-infinite plates, Int. J. Numer. Meth. Engng. **53** (2002) 1145-1173

[20] T. Hayashi, K. Kawashima, Multiple reflections of Lamb waves at a delamination, Ultrasonics, **40**, 193-197 (2002)

[21] N. J. Nigro, Steady-state wave propagation in infinite bars of noncircular cross section, J. Acoust. Soc. Am., **40**, 6, 1501-1508 (1966)

[22] B. Aalami, Waves in prismatic guides of arbitrary cross section, J. Appl. Mech., **40**, 1067-1072 (1973)

[23] H. Taweel, S. B. Dong and M. Kazic, Wave reflection from the free end of a cylinder with an arbitrary cross-section, Int. J. Solids Structures, **37**, 1701-1726 (2000)

[24] L. Gavrić, Computation of propagative waves in free rail using a finite element technique, J. Sound and Vibration, **187**, 3, 531-543 (1995)

[25] L. Gry, Dynamic modelling of railway track based on wave propagation, J. Sound and Vibration, **195**, 3, 477-505 (1996)

[26] D. J. Thompson and C. J. C. Jones, Sound radiation from a vibrating railway wheel, J. Sound and Vibration, **253**, 2, 401-419 (2002)